Since January 2020 Elsevier has created a COVID-19 resource centre with free information in English and Mandarin on the novel coronavirus COVID-19. The COVID-19 resource centre is hosted on Elsevier Connect, the company's public news and information website.

Journal of Hazardous Materials 391 (2020) 121855

Contents lists available at ScienceDirect

Journal of Hazardous Materials

journal homepage: www.elsevier.com/locate/jhazmat

Methylene blue degradation by the VUV/UV/persulfate process: Effect of pH on the roles of photolysis and oxidation

Dong Wen, Wentao Li, Jinrong Lv, Zhimin Qiang, Mengkai Li*

Key Laboratory of Drinking Water Science and Technology, Research Center for Eco-Environmental Sciences, University of Chinese Academy of Sciences, Chinese Academy of Sciences, 18 Shuang-qing Road, Beijing, 100085, China

GRAPHICAL ABSTRACT

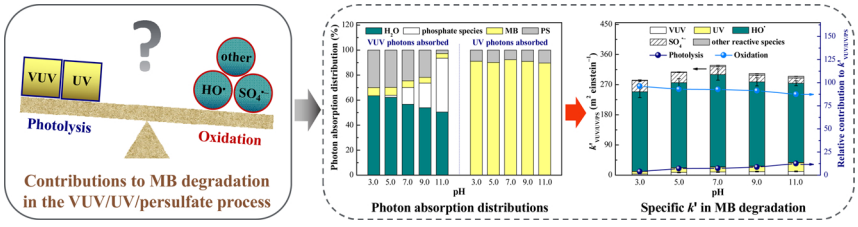

ARTICLE INFO

Editor: Xiaohong Guan

Keywords:
Vacuum ultraviolet (VUV)
VUV/UV/persulfate
Photon absorption distribution
Degradation mechanism
Water treatment

ABSTRACT

This study investigated methylene blue (MB) degradation by the vacuum-ultraviolet/ultraviolet/persulfate (VUV/UV/PS) process using a mini-fluidic VUV/UV photoreaction system. Results show that MB degradation by the VUV/UV/PS process was significantly higher than that of the conventional UV/PS process, as the VUV photolysis of H_2O and PS generated more reactive oxygen species (ROSs). $HO^{\bullet}$ and $SO_4^{\bullet -}$, identified as the main ROSs, were mostly consumed by dissolved organic carbon and Cl^- in real waters, respectively. Additionally, the impacts of solution pH and the concentrations of PS, humic acid, and inorganic ions (HCO_3^-, Cl^-, NO_3^-, SO_4^{2-}, Fe (II), and Fe(III)) were systematically evaluated. The solution pH significantly affected the photon absorption distributions, as well as the contributions of photolysis and oxidation to MB degradation, resulting in different variations in the degradation rate constant and total organic carbon removal ratio with increasing solution pH. At all tested pH levels (3.0–11.0), particularly under acidic conditions, $HO^{\bullet}$ and $SO_4^{\bullet -}$ were two predominant contributors to MB degradation, while VUV and UV photolysis contributed more when the solution pH increased. This study provides a highly efficient process for organic pollutant removal, which could be applied in water treatment.

1. Introduction

Advanced oxidation processes (AOPs) generating highly reactive species (such as $HO^{\bullet}$, $SO_4^{\bullet -}$, and $Cl^{\bullet}$) are among the most efficient and promising chemical oxidation technologies for degrading harmful refractory pollutants that are resistant to conventional water treatment processes, including adsorption, sedimentation, coagulation/flocculation, and sand filtration (Hori et al., 2005; Ling et al., 2016).

Persulfate (PS, a precursor of $SO_4^{\bullet -}$) has a relatively low cost (Lau et al., 2007), high stability in transportation (Waldemer et al., 2007), and an inert and harmless end-product (SO_4^{2-}) (Weiner, 2000); thus, its popularity as a disinfectant or oxidant is increasing. AOPs involving PS activation have been successfully utilized to inactivate microorganisms (such as Coronavirus and Norwalk virus) (Thayer, 2003) and degrade a variety of organic pollutants (McCallum et al., 2000; Lau et al., 2007; Waldemer et al., 2007; Zhang et al., 2016). Ultraviolet (UV), a common

* Corresponding author.
E-mail address: mkli@rcees.ac.cn (M. Li).

https://doi.org/10.1016/j.jhazmat.2019.121855
Received 15 August 2019; Received in revised form 23 November 2019; Accepted 8 December 2019
Available online 09 December 2019
0304-3894/

disinfection and oxidation method, can activate PS (UV/PS process) to produce $SO_4^{\cdot -}$ (Eq. (1)) (Ike et al., 2018), which has a high redox potential ($E^{\circ}_{SO_4^{\cdot -}} = 2.5–3.1$ V) (Neta et al., 1988) that is comparable to or slightly higher than that of $HO^{\cdot}$ ($E^{\circ}_{HO^{\cdot}} = 1.9–2.7$ V) (Buxton et al., 1988). The resulting chain reactions are summarized in Table S1 (Eqs. (S6)–(S14)), and the generated secondary reactive oxygen species (ROSs) mainly include $HO^{\cdot}$, $HO_2^{\cdot}/O_2^{\cdot -}$, $SO_5^{\cdot -}$, and $S_2O_8^{\cdot -}$.

$$S_2O_8^{2-} + h\nu_{254} \rightarrow 2SO_4^{\bullet -} \ (\Phi_{SO_4^{\bullet -}} = 1.4) \quad (1)$$

Low-pressure (LP) mercury lamps are a highly efficient UV light source for water treatment, with a photon-energy efficiency of approximately 36% (Bolton, 2006). By using synthetic silica in the production of the lamp tube, LP mercury lamps can deliver two major resonance lines at 185 and 254 nm (i.e., vacuum-UV (VUV)/UV irradiation), and the manufacturing and operating costs of VUV/UV LP mercury lamps are close to those of a conventional LP mercury lamp (Li et al., 2016). VUV (185 nm) readily photolyzes H_2O into $HO^{\cdot}$ by homolysis and ionization (Eqs. (2) and (3)) (Gonzalez et al., 2004). Moreover, recent studies found that organic pollutant degradation in a UV/chlorine process when a VUV/UV lamp was used as the light source (VUV/UV/chlorine process) was more efficient than that of conventional UV irradiation (UV/chlorine process) owing to the additional formation of $HO^{\cdot}$ (Eqs. (2) and (3)) (Gonzalez et al., 2004) and the synergistic effect (Li et al., 2016). Therefore, VUV/UV LP mercury lamps could serve as a highly efficient light source for UV-based AOPs. However, the application of the VUV/UV/PS process in water treatment has not been studied. Thus, it is necessary to explore organic pollutant degradation by this highly efficient AOP.

$$H_2O + h\nu_{185} \rightarrow HO^{\bullet} + H^{\bullet} \ (\Phi_{HO^{\bullet}} = 0.33) \quad (2)$$

$$H_2O + h\nu_{185} \rightarrow HO^{\bullet} + H^{+} + e^{-}_{aq} \ (\Phi_{HO^{\bullet}} = 0.045) \quad (3)$$

As a cationic dye, methylene blue (MB) that is hard to degrade by traditional technologies can cause various potential health risks to humans and induce significant problems to ecological systems (Bulut and Aydın, 2006; Bedin et al., 2016). The removal kinetics and mechanisms of MB under different conditions (such as various impact factors and real waters) using chemical (Qi et al., 2015; Li et al., 2016; Wolski and Ziolek, 2018; Ren et al., 2019) and physical technologies (Bulut and Aydın, 2006; Qi et al., 2015; Bedin et al., 2016; Wolski and Ziolek, 2018; Ren et al., 2019) have been discussed with drawbacks of the generation of iron sludge, difficulties in separation and regeneration of catalysts, membrane fouling, and high cost. UV-based AOPs were found to be highly efficient for removing MB, which is commonly used as a model organic pollutant (Bulut and Aydın, 2006; Qi et al., 2015; Bedin et al., 2016; Li et al., 2016; Wolski and Ziolek, 2018; Ren et al., 2019) with good stability under UV irradiation and easy detection. Moreover, when combined with the previously developed mini-fluidic VUV/UV photoreaction system (MVPS; Fig. S1) (Li et al., 2016), MB concentration can be measured precisely and rapidly with an online UV–vis spectrophotometer during its degradation in the UV-based AOPs, which could avoid sampling errors and reduce the workload.

In this study, we aimed to investigate MB degradation kinetics by the VUV/UV/PS process based on the MVPS, which was found to be suitable for estimating the impact of VUV on organic pollutant degradation during VUV/UV irradiation. The effects of solution pH and water matrix components were assessed, and the main ROSs and their consumption distributions in different types of real water were elucidated. Additionally, the pH impact on the photon absorption distributions was explored to understand the roles of direct photolysis (VUV and UV) and indirect oxidation by various oxidants at different pH levels. This study proposes a new UV-based AOP for water treatment, which could be used for highly efficient organic pollutant removal.

2. Materials and methods

2.1. Chemicals and water samples

All chemical reagents were of analytical grade or higher. Anisole (AS), methanol (MeOH), *p*-chlorobenzoic acid (*p*CBA), and potassium persulfate ($K_2S_2O_8$) were purchased from Thermo Fisher Scientific, Inc. (USA), while MB, *tert*-butyl alcohol (TBA), and uridine were supplied by Sigma-Aldrich, Inc. (USA). Humic acid (HA) and H_3PO_4 (≥ 85% w/w) were obtained from Aladdin Bio-Chem Technology Co., Ltd. (China). The other reagents were purchased from Sinopharm Chemical Reagent Co., Ltd. (China). All solutions were prepared with ultrapure water (resistivity > 18.2 MΩ cm) produced by a Milli-Q water purification system (Advantage A10, Millipore, USA).

Filtered water (FW), surface water (SW), and secondary wastewater effluent (WE) were collected from a local drinking water treatment plant, an urban river, and a municipal wastewater treatment plant, respectively (Beijing, China). All water samples were immediately transported to the laboratory in a portable refrigerator, vacuum-filtered through 0.45-μm membrane filters to remove any particles, and stored at 4 °C prior to analysis and testing.

2.2. Experimental procedures

All photochemical experiments were conducted at least thrice in the MVPS (Fig. S1), the structure of which was described in a previous study (Li et al., 2016). The flow rate was 60 mL min^{-1} and the reaction solution temperature was maintained at 25 °C using a water recirculator (DHX-0515, Shunma Technology Co., China). The solution pH was adjusted using various solutions (H_3PO_4, NaH_2PO_4, Na_2HPO_4, and Na_3PO_4) with total phosphate concentrations of 2.0 mM, unless otherwise stated. During the total organic carbon (TOC) tests, solution samples were withdrawn and quenched with excess $Na_2S_2O_3$ before analysis. Using MeOH and uridine as chemical actinometers, the VUV (E^{o}_{p},VUV) and UV (E^{o}_{p},UV) photon fluence rates were measured to be 2.59×10^{-5} and 5.31×10^{-4} einstein m^{-2} s^{-1}, respectively (Fig. S2). As the reaction solution was recirculated between unexposed (Teflon connection tube wrapped in black tape) and exposed (VUV/UV or UV tube) sections of the MVPS, a reduction equivalent exposure time (t_{ree}, s) was determined as the total reaction time (t, 600 s) multiplied by the ratio of the exposed volume of the operation tube ($\pi r^2 l$, cm^3) to the total volume of the reaction solution (V, 100 cm^3) (Wen et al., 2018). Therefore, the VUV ($F_{p,VUV}$), UV ($F_{p,UV}$), and total ($F_{p,tot}$) photon fluences (einstein m^{-2}) can be calculated as follows (Li et al., 2016):

$$t_{ree} = \frac{\pi r^2 l}{V} t \quad (4)$$

$$F_{p,VUV} = E^{o}_{p},VUV t_{ree} \quad (5)$$

$$F_{p,UV} = E^{o}_{p},UV t_{ree} \quad (6)$$

$$F_{p,tot} = F_{p,VUV} + F_{p,UV} \quad (7)$$

where r and l are the radius and length of the VUV/UV or UV tube (cm), respectively.

2.3. Analytical methods

The solution pH was measured using an EF-20 K pH meter (Mettler, Switzerland). UV_{254} and the concentrations of uridine and MB were quantified at 254, 262, and 664 nm, respectively, using a UV–vis spectrometer (UV-2600, Shimadzu, Japan). The alkalinity was determined using a DR6000 UV–vis spectrometer (Hach, USA) following the Hach method 8203. The TOC concentration was analyzed with a TOC analyzer (TOC-$V_{CPH/CPN}$, Shimadzu, Japan), while the Cl^-, NO_2^-, NO_3^-, and SO_4^{2-} concentrations were determined by an ICS-2100 ion chromatograph (Dionex, USA) equipped with an AS19-HC anion-

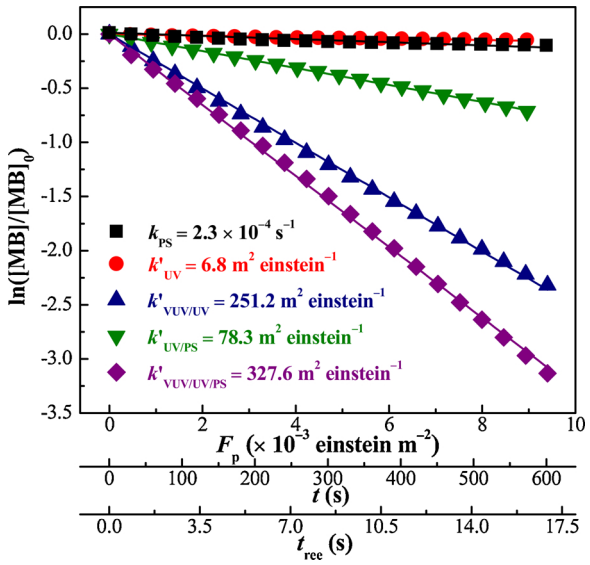

Fig. 1. MB degradation in the PS, UV, VUV/UV, UV/PS, and VUV/UV/PS processes. Experimental conditions: $[MB]_0$ = 10 μM, $[PS]_0$ = 0.5 mM, pH = 7.0, temp. = 25 °C.

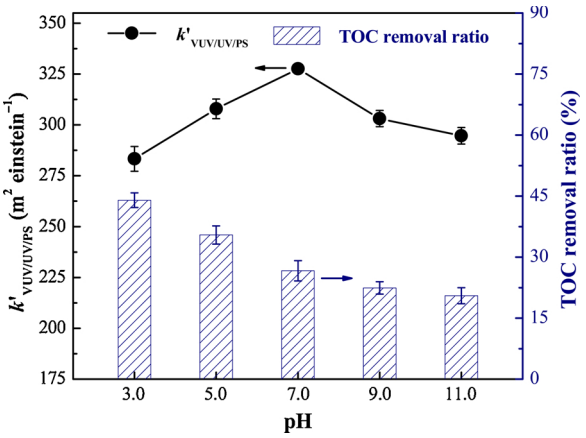

Fig. 2. Effect of pH on the degradation rate constants and mineralization of MB in the VUV/UV/PS process. Experimental conditions: $[MB]_0$ = 10 μM, $[PS]_0$ = 0.5 mM, temp. = 25 °C, reaction time = 10 min.

separation column (4.0 × 250 mm, 5 μm). The AS and MeOH concentrations were measured using a gas chromatograph equipped with a flame ionization detector (2010 Plus, Shimadzu, Japan) and an Rtx-Wax column (30 m × 0.25 mm, 0.25 μm) (Shimadzu, Japan) (Text S1). The *p*CBA concentration was quantified at 230 nm with a high-performance liquid chromatograph (Agilent 1200, USA) equipped with a UV detector and an Atlantis® dC18 column (4.6 × 250 mm, 5 μm) (Waters, USA) (Text S1). In all figures, the relative standard deviations for all data points is less than 5%, and the error bars represent the standard deviations (n = 3).

3. Results and discussion

3.1. MB degradation kinetics in the VUV/UV/PS process

Fig. 1 shows that the MB degradation of all five processes could be fitted well with pseudo-first-order kinetics. Although PS is typically considered as a strong oxidant ($E^{\circ}_{S_2O_8^{2-}}$ = 2.01 V) (Gao et al., 2012) and MB has a high molar absorption coefficient at 254 nm ($\varepsilon_{MB,254}$ = 1.18 × 10^4 M^{-1} cm^{-1}; Fig. S3), MB degradation by both direct PS oxidation (k_{PS} = 2.3 × 10^{-4} s^{-1}) and direct UV photolysis (k'_{UV} = 6.8 m^2 einstein^{-1}) was very low. However, the UV/PS process significantly increased the reaction rate constant ($k'_{UV/PS}$ = 78.3 m^2 einstein^{-1}) because of the formation of $SO_4^{\bullet-}$ (Eq. (1)) (Ike et al., 2018) and HO$^{\bullet}$ (Eq. (S7); Table S1). Rapid MB degradation was observed in the VUV/UV process ($k'_{VUV/UV}$ = 251.2 m^2 einstein^{-1}), which generated HO$^{\bullet}$ from the VUV photolysis of H_2O (Eqs. (2) and (3)) (Gonzalez et al., 2004). After adding PS, MB degradation during the VUV/UV/PS process ($k'_{VUV/UV/PS}$) was significantly higher than that under VUV/UV irradiation owing to the additional indirect oxidation by $SO_4^{\bullet-}$ generated during the VUV and UV photolysis of PS. Additionally, $k'_{VUV/UV/PS}$ (327.6 m^2 einstein^{-1}) was 3.2 times higher than $k'_{UV/PS}$ as more ROSs were produced by the VUV photolysis of H_2O and PS.

3.2. Effect of pH

As an important impact factor, the solution pH has been reported to notably affect the acid-base speciation of solutes (such as organic pollutants and oxidants) and other physicochemical properties of solution (Guan et al., 2011; Xie et al., 2015). Therefore, $k'_{VUV/UV/PS}$ and TOC removal ratio in the VUV/UV/PS process at different pH levels were studied and are shown in Fig. 2. $k'_{VUV/UV/PS}$ increased within a pH range of 3.0–7.0, and then decreased as the solution pH further increased from 7.0 to 11.0; the highest $k'_{VUV/UV/PS}$ was observed at pH 7.0. However, the TOC removal ratio steadily decreased with increasing solution pH. The required levels of target parent pollutant and TOC (or chemical oxygen demand) removal in practical water treatment differ. Therefore, it is necessary to elucidate the mechanisms behind the different trends of $k'_{VUV/UV/PS}$ and TOC removal ratio at various pH levels, which could be useful for selecting an economic treatment strategy according to the specific requirements of a certain scenario (this is discussed in detail in Section 3.6).

3.3. Effects of PS and water matrix components

Fig. 3 shows that the $k'_{VUV/UV/PS}$ obviously increased with increasing PS dose from 0.1 to 1.5 mM. With increasing PS dose, despite more HO$^{\bullet}$ and/or $SO_4^{\bullet-}$ were consumed (Eqs (S6), (S9), (S10), and (S11); Table S1), $SO_4^{\bullet-}$ formation by the photolysis (VUV and UV) of PS and the reaction of HO$^{\bullet}$ with PS (Eq. (S10); Table S1) was enhanced, thus leading to a higher $k'_{VUV/UV/PS}$ value.

As shown in Fig. 3, all water matrix components inhibited MB degradation, excluding Fe(II) and Fe(III) at relatively low concentrations (≤ 5.0 μM). The level of inhibition by each component decreased in the following order: HA > Cl^- > NO_3^- > HCO_3^- > SO_4^{2-} > Fe(III) > Fe(II) (see the inset in Fig. 3).

HA greatly decreased $k'_{VUV/UV/PS}$ by filtering VUV and UV light ($\varepsilon_{HA,185}$ < 2.13 × 10^{-5} and $\varepsilon_{HA,254}$ = 3.01 × 10^{-5} M_C^{-1} cm^{-1}; Fig. S4), consuming PS, and scavenging ROSs ($k_{HA,HO^{\bullet}}$ = 3.90 × 10^8 and $k_{HA,SO_4^{\bullet-}}$=2.35 × 10^7 M_C^{-1} s^{-1}; Table S2) (Brezonik and Fulkerson-Brekken, 1998; Xie et al., 2015). Although UV could activate HA to generate different reactive species (such as $^1O_2$ and e^-_{aq}) (Latch and McNeill, 2006; Zhang and Hsu-Kim, 2010; Xie et al., 2015), their contributions to MB degradation were assumed to be ignored herein.

Four typical anions (HCO_3^-, Cl^-, NO_3^-, and SO_4^{2-}) were also found to inhibit MB degradation. All added anions and/or their transformations (such as H_2CO_3, CO_3^{2-}, and NO_2^-) rapidly reacted with HO$^{\bullet}$ and/or $SO_4^{\bullet-}$ at rate constants ranging from 2.1 × 10^6 to 1.4 × 10^{10} M^{-1} s^{-1} (Table S2) (Buxton et al., 1988; Li et al., 2016), which could produce secondary reactive species (such as $CO_3^{\bullet-}$, $Cl_2^{\bullet-}$, and $NO_3^{\bullet}$) with lower reactivities, thereby reducing MB removal. Additionally, anions and their transformations could also compete with other solution components (such as H_2O, MB, and PS) for VUV and UV photons (Fig. S4), hence weakening ROS generation and MB degradation by direct photolysis.

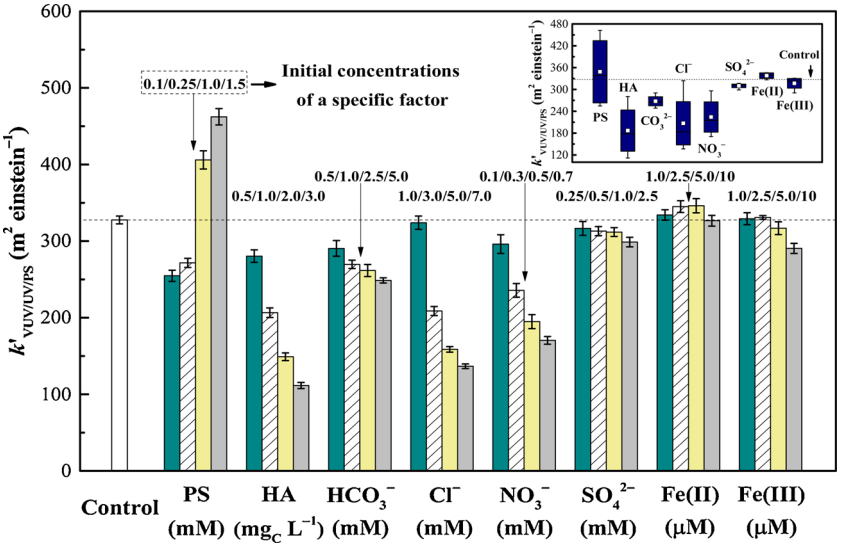

Fig. 3. Effects of PS and water matrix components on MB degradation rate constants in the VUV/UV/PS process. Experimental conditions of control test: $[MB]_0$ = 10 μM, $[PS]_0$ = 0.5 mM, pH = 7.0, temp. = 25 °C, reaction time = 10 min.

Iron is one of the most common transition metals in aquatic environments. Fig. 3 shows that the addition of 1.0–5.0 μM Fe(II) or 1.0–2.5 μM Fe(III) slightly increased $k'_{VUV/UV/PS}$, because more ROSs could be generated in the presence of low iron concentrations (Eqs. (S15)–(S18); Table S1). However, higher Fe(II) (>5.0 μM) or Fe(III) (>2.5 μM) concentrations negatively affected $k'_{VUV/UV/PS}$, which could be attributed to the high level of $HO^{\bullet}$ and $SO_4^{\bullet-}$ scavenging by iron (Eqs. (S19) and (S20); Table S1) (Anipsitakis and Dionysiou, 2004; Rastogi et al., 2009) and competition for VUV and UV photons (Fig. S4).

3.4. Identification of the principal ROSs and the measurement of $k_{HA,HO^{\bullet}}$ and $k_{HA,SO_4^{\bullet-}}$

To identify the primary ROSs and quantify their contributions to MB degradation, specific quenching experiments were conducted. Four possible ROSs were formed during the VUV/UV/PS process ($HO^{\bullet}$, $HO_2^{\bullet}/O_2^{\bullet-}$, $SO_4^{\bullet-}$, and $SO_5^{\bullet-}$; Eqs. (1)–(3) and (S6)–(S14); Table S1). MB degradation by indirect $HO_2^{\bullet}/O_2^{\bullet-}$ and $SO_5^{\bullet-}$ oxidation was negligible because of their relatively low E^o values ($E^{\circ}_{HO_2^{\bullet}} > 1.0$, $E^{\circ}_{O_2^{\bullet-}} 1 = 0.57 \pm 0.01$, and $E^{\circ}_{SO_5^{\bullet-}} = 1.1$ V) (Rao and Hayon, 1973; Gilbert and Stell, 1990). TBA was selected as a scavenger for $HO^{\bullet}$ owing to its high rate constant with $HO^{\bullet}$ ((3.8–7.6) × 10^8 M^{-1} s^{-1}; Table S2) and low rate constant with $SO_4^{\bullet-}$ ((4.0–9.1) × 10^5 M^{-1} s^{-1}; Table S2) (Anipsitakis and Dionysiou, 2004). As it shares high rate constants with both $HO^{\bullet}$ (9.7 × 10^8 M^{-1} s^{-1}; Table S2) (Buxton et al., 1988) and $SO_4^{\bullet-}$ (2.5 × 10^7 M^{-1} s^{-1}; Table S2) (Neta et al., 1988), MeOH was used to effectively scavenge both of these ROSs.

Fig. S5a shows that $k'_{VUV/UV/PS}$ considerably decreased from 327.6 to 52.4 and 29.2 m^2 $einstein^{-1}$ in the presence of 100 mM of TBA and 100 mM of MeOH, respectively. This indicates that $HO^{\bullet}$ and $SO_4^{\bullet-}$ were the two main ROSs accountable for MB degradation, and the former played a more significant role in the VUV/UV/PS process. However, as for the UV/PS process, $SO_4^{\bullet-}$ rather than $HO^{\bullet}$ was identified as the dominating ROS responsible for the degradation of pharmaceuticals and the formation of chlorate (Lian et al., 2017; Hou et al., 2018). During MB degradation in the VUV/UV/PS process, the relative contributions of $HO^{\bullet}$ and $SO_4^{\bullet-}$ oxidation were 84.0% and 7.1%, respectively, and the remaining 8.9% can be attributed to direct photolysis by VUV and UV irradiation, and oxidation by PS, $HO_2^{\bullet}/O_2^{\bullet-}$ and $SO_5^{\bullet-}$.

The second-order rate constants of MB with $HO^{\bullet}$ ($k_{MB,HO^{\bullet}}$) and $SO_4^{\bullet-}$ ($k_{MB,SO_4^{\bullet-}}$) were determined by calculating the competition kinetics using *p*CBA ($k_{pCBA,HO^{\bullet}}$ = 5.0 × 10^9 M^{-1} s^{-1}; Table S2) (Kutschera et al., 2009) and AS ($k_{AS,SO_4^{\bullet-}}$ = 4.9 × 10^9 M^{-1} s^{-1}; Table S2) (O'Neill et al., 1975) as reference compounds, respectively. Detailed information regarding this is provided in Text S2. Based on the reaction rate constant ratios of $k_{MB,HO^{\bullet}}$ to k_PCBA, $HO^{\bullet}$ (0.760) and $k_{MB,SO_4^{\bullet-}}$ to $k_{AS,SO_4^{\bullet-}}$ (0.623) (Fig. S5b), $k_{MB,HO^{\bullet}}$ and $k_{MB,SO_4^{\bullet-}}$ were calculated to be 3.8 × 10^9 and 3.1 × 10^9 M^{-1} s^{-1}, respectively.

3.5. Performance of the VUV/UV/PS process and ROS consumption distributions in various real waters

To assess the practical performance of the VUV/UV/PS process, MB was used as a model organic pollutant and added to three real waters (FW, SW, and WE), the sources and major water quality parameters of which are summarized in Table S3. Fig. S6 shows that $k'_{VUV/UV/PS}$ in FW, SW, and WE were 0.6%, 6.4%, and 21.7% lower than that in Milli-Q water. This demonstrates that the VUV/UV/PS process would be feasible for organic pollutant degradation removal in practice.

The consumption distributions of $HO^{\bullet}$ and $SO_4^{\bullet-}$ among the major matrix components in different water samples during MB degradation by the VUV/UV/PS process were calculated using Eq. (8) (Lian et al., 2017) (Fig. 4).

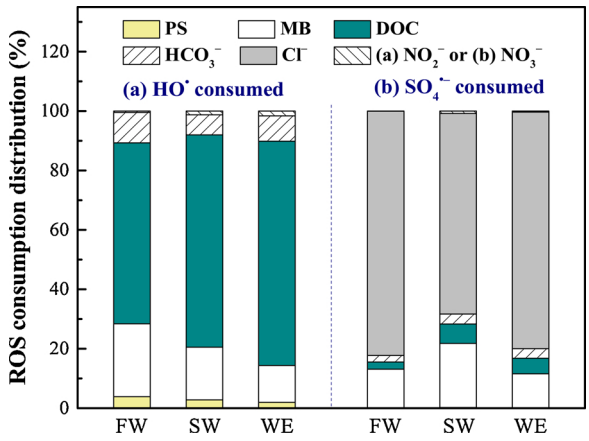

Fig. 4. Fractions of $HO^{\bullet}$ (a) and $SO_4^{\bullet-}$ (b) consumed by major matrix components during MB degradation in various waters using the VUV/UV/PS process. Experimental conditions: $[MB]_0$ = 10 μM, $[PS]_0$ = 0.5 mM, temp. = 25 °C.

$$R_{i,j} = \frac{k_{i,j}C_j}{\sum_{j=1}^{j} k_{i,j}C_j} \times 100 \quad (8)$$

where $R_{i,j}$ and $k_{i,j}$ are the ROS consumption fraction (%) and second-order rate constant ($M^{-1}\ s^{-1}$ or $M_C{}^{-1}\ s^{-1}$) of a certain ROS (i) with a specific water component (j), respectively, and C_j is the molar concentration (M or M_C) of j.

Fig. 4a shows that 60.9%–75.5% of $HO^{\bullet}$ reacted with dissolved organic carbon (DOC), indicating the DOC of each water sample significantly affected the $k'_{VUV/UV/PS}$ value. The addition of HA (1.0–3.0 $mg_C\ L^{-1}$) resulted in a larger decrease in $k'_{VUV/UV/PS}$ (Fig. 3) than that caused by the DOC (2.9–7.1 $mg_C\ L^{-1}$; Table S3) contained in the water samples (Fig. S6). This could be due to the higher reaction rate constants between HA and ROSs (such as $HO^{\bullet}$ and $SO_4^{\bullet-}$) than those between the DOC contained in the water samples and ROSs (Xie et al., 2015; Li et al., 2018). Mckay et al. (2011) also observed that the reaction rate constants between organic matter and $HO^{\bullet}$ ranged from 1.21×10^8 to $9.37 \times 10^8\ M^{-1}\ s^{-1}$ because of variations in the properties of organic matter.

PS and HCO_3^- scavenged 2.0%–3.9% and 6.8%–10.2% of $HO^{\bullet}$ to generate $SO_4^{\bullet-}$ and $CO_3^{\bullet-}$, respectively. Although it was present in relatively high concentrations (0.318–0.707 mM; Table S3), the fraction of $HO^{\bullet}$ consumed by Cl^- can be neglected as the reactions were reversible (Eqs. (9) and (10)) (Jayson et al., 1973; Yang et al., 2014), which had a net rate of $10^3\ M^{-1}\ s^{-1}$ at pH 7.0 that decreased by 90% per increasing pH unit (Von Gunten, 2003).

$$Cl^- + HO^{\bullet} \rightarrow Cl^{\bullet} + OH^- \ (k = 4.3 \times 10^9\ M^{-1}\ s^{-1}) \quad (9)$$

$$Cl^{\bullet} + OH^- \rightarrow Cl^- + HO^{\bullet} \ (k = 6.1 \times 10^9\ M^{-1}\ s^{-1}) \quad (10)$$

However, Fig. 4b shows that there was a considerable difference in the consumption distributions of $SO_4^{\bullet-}$ and $HO^{\bullet}$. Cl^- (67.5%–82.2%) was the main component responsible for $SO_4^{\bullet-}$ consumption, followed by MB (11.4%–21.6%). DOC and HCO_3^- scavenged less than 10% of the $SO_4^{\bullet-}$. Additionally, the $SO_4^{\bullet-}$ fractions consumed by PS and NO_3^- with rate constants of 6.1×10^5 and $2.1 \times 10^6\ M^{-1}\ s^{-1}$ (Table S2) (Neta et al., 1988; Buxton et al., 1999), respectively, were negligible (0.2 %–1.0%).

3.6. Photon absorption distributions and degradation mechanisms at different pH levels

3.6.1. Photon absorption distributions at different pH levels

Fig. 2 shows that the trends of $k'_{VUV/UV/PS}$ and TOC removal ratio differed as the solution pH increased. The solution pH can affect the dissociation of $H_3PO_4/H_2PO_4^-/HPO_4^{2-}/HPO_4^{3-}$ ($pK_{a1} = 2.1$, $pK_{a2} = 7.2$, and $pK_{a3} = 12.3$) (Pan et al., 2017) and $MB^+/MB^0/MB^-$ ($pK_{a1} = 2.6$ and $pK_{a2} = 11.2$; MB^+, MB^0, and MB^- represent the cationic, neutral, and anionic species, respectively) (Huang et al., 2010), thereby altering their optical properties and reactivities. The VUV and UV photon absorption distributions among the solution components (H_2O, phosphate species, MB, and PS) at various pH levels were calculated following the methods that were described in a previous study (Wen et al., 2018), and are shown in Fig. 5a.

Under a strongly acidic condition (pH 3.0), 63.4% of the VUV photons were trapped by H_2O due to its high concentration (approximately 55.6 M) and large $\varepsilon_{H_2O,185}$ (Zoschke et al., 2014), and 30.0 % of the VUV photons were absorbed by PS. Therefore, most of the VUV photons participated in the photodecomposition of H_2O and PS to yield $HO^{\bullet}$ and $SO_4^{\bullet-}$, respectively, during the VUV/UV/PS process, rather than partaking in the direct photolysis of MB, which absorbed 6.6% of the VUV photons. As the solution pH increased from 3.0 and 7.0 to 11.0, the fractions of VUV photons absorbed by the phosphate species increased from 0% and 13.4%–43.1%, while the fractions of those absorbed by H_2O, MB, and PS decreased from 63.4% and 56.7%–50.4%, from 6.6% and 5.4% to 3.8%, and from 30.0% and 24.5% to 2.7%, respectively. As the photoactivation of phosphate species forms weak oxidants ($H_2PO_4^{\bullet}$ and $HPO_4^{\bullet-}$) (Crittenden et al., 1999), this process was insignificant during MB degradation. Therefore, more VUV photons were captured by phosphate species with increasing solution pH, which resulted in the lower effective absorption of VUV photons by H_2O, MB, and PS at a higher pH.

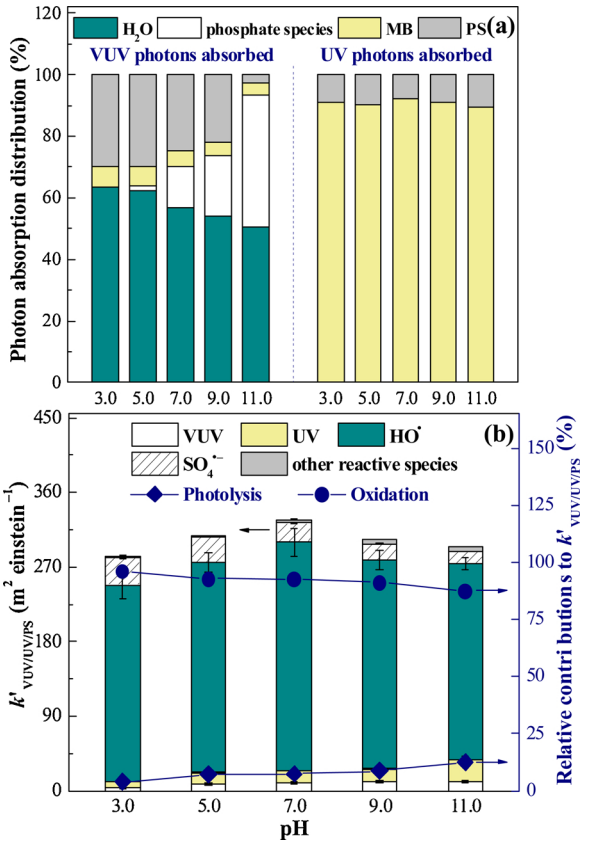

Fig. 5. Fractions of VUV and UV photons absorbed by each solution component (a) as well as contributions of photolysis (VUV and UV) and oxidation ($HO^{\bullet}$, $SO_4^{\bullet-}$, and other reactive species) to MB degradation (b) as a function of pH in the VUV/UV/PS process. Experimental conditions: $[MB]_0 = 10\ \mu M$, $[PS]_0 = 0.5$ mM, temp. = 25 °C, reaction time = 10 min [only for (b)].

Unlike the VUV photon absorption distributions, the UV photon absorption distributions were almost pH-independent. Neither H_2O nor phosphate species could consume UV photons. Approximately 89.6%–92.3% and 7.7%–10.4% of the UV photons were absorbed by MB and PS, respectively, indicating that most of the UV photons were utilized in the direct photolysis of MB, rather than the photoactivation of PS.

Taking into consideration the fractions of both VUV and UV photons absorbed by each solution component, it is reasonable to expect that the dominant degradation mechanism could differ at various pH levels (i.e., the solution pH would affect the contributions of direct photolysis and indirect oxidation to MB degradation).

3.6.2. Degradation mechanisms at different pH levels

To quantitatively estimate the roles of photolysis and oxidation in MB degradation at different pH levels, the specific reaction rate constants for MB degradation by VUV photolysis (k'_{VUV}), UV photolysis (i.e., k'_{UV}), $HO^{\bullet}$ oxidation ($k'_{HO^{\bullet}}$), $SO_4^{\bullet-}$ oxidation ($k'_{SO_4^{\bullet-}}$), and oxidation by other reactive species (k'_{other}) at various pH levels were determined (Fig. 5b) following the methods described in Text S3.

Fig. 5b shows that most of the MB was oxidized by $SO_4^{\bullet-}$ and $HO^{\bullet}$. With an increase in the solution pH, $k'_{SO_4^{\bullet-}}$ significantly decreased from 33.4 to 15.0 $m^2\ einstein^{-1}$; while $k'_{HO^{\bullet}}$ was 6.1–14.7 times higher than

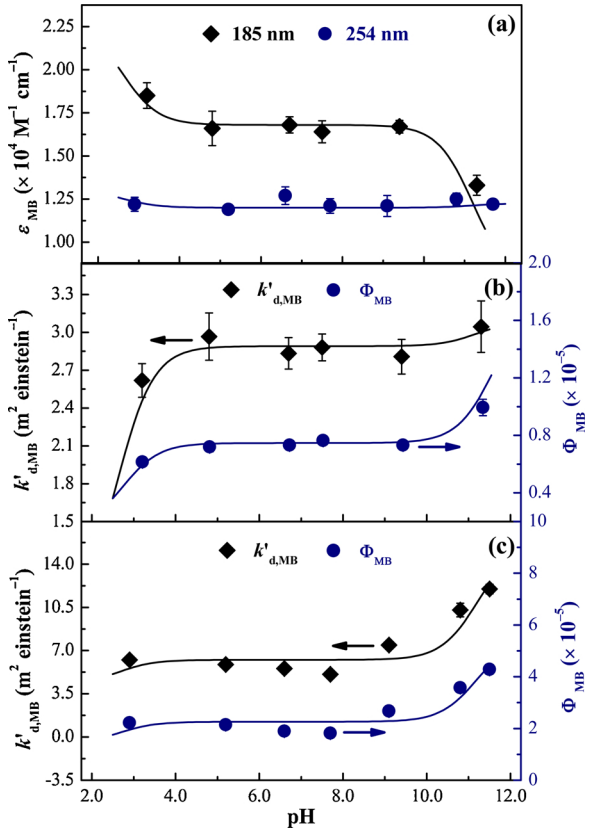

Fig. 6. Molar absorption coefficients of MB (ε_{MB}) at both 185 and 254 nm (a) as well as pseudo-first-order rate constants ($k'_{d,MB}$) and quantum yields (Φ_{MB}) of MB by direct VUV (b) and UV (c) photolysis as a function of pH. Experimental conditions: $[MB]_0$ = 10 μM, $[TBA]_0$ = 100 mM [only for (b)], temp. = 25 °C, reaction time = 10 min. The symbols and curves represent experimental data and model-fitting results, respectively.

$k'_{SO_4^{\bullet-}}$ at each pH level, and initially increased (pH 3.0–7.0), but then decreased (pH 7.0–11.0). The acceleration of the reaction rate between $SO_4^{\bullet-}$ and HO^- (Eq. (S8); Table S1) with increasing solution pH largely accounted for the decreased contribution of $SO_4^{\bullet-}$ (from 11.8% to 5.1%) to MB degradation. However, for $k'_{HO^\bullet}$, increasing solution pH enhanced $HO^\bullet$ generation by reducing $SO_4^{\bullet-}$ concentration (Eqs. (S7) and (S8); Table S1) and weakened the scavenging effect of H^+ on $HO^\bullet$ (Tang and Huang, 1996). Meanwhile, $E^\circ_{HO^\bullet}$ declined as the solution pH increased (Kim and Vogelpohl, 1998). Additionally, the concentration of HPO_4^{2-}, which could react with ROSs more rapidly than the reaction between $H_2PO_4^-$ and ROSs (Table S2) (Pan et al., 2017), was higher under alkaline conditions, thereby decreasing the concentrations of ROSs. As a result, the minimum and maximum $k'_{HO^\bullet}$ (236.5 and 275.3 m^2 einstein^{-1}) values were observed at pH 11.0 and 7.0, respectively.

As shown in Fig. 5b, the k'_{VUV} and k'_{UV} values increased from 3.1 to 11.2 m^2 einstein^{-1} and from 7.8 to 25.7 m^2 einstein^{-1}, respectively, with increasing solution pH. To evaluate the pH-dependence, ε_{MB} and the direct photolysis rate constants of MB ($k'_{d,MB}$) were determined at various pH levels (Fig. 6). $\varepsilon_{MB,185}$ clearly decreased within pH ranges of 3.2–4.8 and 9.4–11.3, but remained almost unchanged at other pH levels; while $\varepsilon_{MB,254}$ was almost pH-independent (Fig. 6a). The variations in ε_{MB} with the solution pH were modeled by assigning each existing species to a specific ε (ε_{MB^+}, ε_{MB^0}, ε_{MB^-}). The apparent absorbance of MB solution was equal to the sum of absorbance attributed to each existing species (Eq. (11)) (Canonica et al., 2008).

$$\varepsilon_{MB} = \varepsilon_{MB^+}\alpha_{MB^+} + \varepsilon_{MB^0}\alpha_{MB^0} + \varepsilon_{MB^-}\alpha_{MB^-} \quad (11)$$

where α_{MB^+}, α_{MB^+}, and α_{MB^-} are the distribution coefficients of MB^+, MB^0, and MB^-, respectively. The results in Fig. 6a indicate that the modeling results agreed well with the experimental data. ε_{MB^+}, ε_{MB^0}, and ε_{MB^-} were calculated and are shown in Table 1.

Table 1
Specific kinetic parameters for direct VUV and UV photolysis of MB in aqueous solution.

λ (nm)	ε ($\times 10^4$ M^{-1} cm^{-1})			k'_d (m^2 einstein^{-1})			Φ ($\times 10^{-5}$)		
	MB^+	MB^0	MB^-	MB^+	MB^0	MB^-	MB^+	MB^0	MB^-
185	2.28	1.68	0.78	0.73	2.89	3.09	0.14	0.75	1.72
254	1.31	1.20	1.23	4.19	6.29	15.49	1.40	2.21	5.47

The $k'_{d,MB}$ values determined under VUV and UV irradiation, which increased with increasing solution pH, are shown in Fig. 6b and c. The specific k'_d value of each existing species (k'_{d,MB^+}, k'_{d,MB^0}, and k'_{d,MB^-}) was obtained by Eq. (12) (Lian et al., 2015) (Table 1).

$$k'_{d,MB} = k'_{d,MB^+}\alpha_{MB^+} + k'_{d,MB^0}\alpha_{MB^0} + k'_{d,MB^-}\alpha_{MB^-} \quad (12)$$

k'_{d,MB^-} was higher than k'_{d,MB^+} and k'_{d,MB^0}, which was similar to the results of k'_{UV} and k'_{VUV} presented in Fig. 5b. The quantum yields (Φ) of each existing species (Φ_{MB^-}, Φ_{MB^0}, and Φ_{MB^+}) could be readily calculated using Eq. (13) (Bolton and Stefan, 2002), and are presented in Table 1. The Φ values at both 185 and 254 nm decreased in the order of: $\Phi_{MB^-} > \Phi_{MB^0} > \Phi_{MB^+}$.

$$\Phi = \frac{k'_d}{10 \times \ln 10 \times \varepsilon} \quad (13)$$

The contributions of oxidation by PS and other reactive species to MB degradation could be ignored. Therefore, the maximum apparent $k'_{VUV/UV/PS}$ value (i.e., the summation of various k' values) was observed at pH 7.0. Under the tested pH of 3.0–11.0, indirect $HO^\bullet$ and $SO_4^{\bullet-}$ oxidation mainly contributed to MB degradation. However, with an increase in the solution pH, the roles of direct VUV and UV photolysis became more important. As indirect oxidation was more effective for mineralizing MB and its intermediate products than direct photolysis, the above analysis of the effect of pH on the degradation mechanism can explain the different trends of the variations in MB degradation (discoloration) and TOC removal with increasing solution pH (Fig. 2).

3.7. Potential applications

The results in Fig. 1 indicate that the $k'_{VUV/UV/PS}$ was almost the same as the sum of $k'_{VUV/UV}$ and $k'_{UV/PS}$, suggesting that the synergistic enhancement of organic pollutant degradation observed in the VUV/UV/chlorine process (Li et al., 2016, 2018) did not occur in the VUV/UV/PS process. However, owing to the similar manufacturing costs and power inputs of VUV/UV and conventional LP mercury lamps, the organic pollutant removal efficiency and water treatment cost of the VUV/UV/PS process could be better than those of the UV/PS process. The evaluation of energy consumption for various treatment processes was detailed in Text S4 and the electrical energy per order value of 0.347 kW h m^{-3} order^{-1} (Table S4) suggest a good application potential of the VUV/UV/PS process in effectively degrading organic pollutants.

Additionally, it is found that the trends of $k'_{VUV/UV/PS}$ and the TOC removal ratio with increasing solution pH in the VUV/UV/PS process differed (Fig. 2), and the mechanism was elucidated. This approach could be used to develop an economic treatment strategy (such as adjusting the solution pH before treating organic pollutants by the VUV/UV/PS process) in practical water treatment according to the specific requirements (parent compound or TOC elimination), target organic pollutant properties, and practical water matrices.

4. Conclusions

In this study, MB degradation in an aqueous solution by the VUV/UV/PS process was investigated. The following conclusions can be drawn from the experimental results:

- MB degradation by the VUV/UV/PS process was more rapid than that in the conventional UV/PS process. Increasing PS dose enhanced MB degradation, while the addition of HA, HCO_3^-, Cl^-, NO_3^-, and SO_4^{2-} inhibited MB degradation to different degrees. The effects of Fe(II) and Fe(III) were dependent on the iron concentrations.
- Unlike the steady decrease in the TOC removal ratio, $k'_{VUV/UV/PS}$ first increased and then decreased with increasing solution pH. This is because various pH levels induced different roles of photolysis and oxidation. Increasing solution pH increased the contributions of direct VUV and UV photolysis to MB degradation, but were ineffective in mineralizing MB and its intermediate products.
- $HO^{\bullet}$ and $SO_4^{\bullet-}$ were identified as the two dominant ROSs and were mainly consumed by the DOC and Cl^- in real waters, respectively. The tests conducted in real waters demonstrate that the VUV/UV/PS process has a good potential for highly efficient removal of organic pollutant in practice.
- As the parent compound and TOC are two different objects for removal in water treatment, this study may provide an economic treatment strategy that can be adjusted according to the specific requirements of a certain scenario.

Author contributions

Dong Wen: The first author: completing most of the experiments, analyzing experimental data, and writing article.

Wentao Li: The second author: lab assistant.

Jinrong Lv: The third author: lab assistant.

Zhimin Qiang: The fourth author: proposing research direction, guiding experiment, and modifying article.

Mengkai Li: The fifth and corresponding author: providing research approach, guiding experiment, and modifying article.

Declaration of Competing Interest

The authors declare that the work under consideration for publication was only supported by government funding agencies. There is no any conflict of interest outside of the submitted work. Contents of this work do not necessarily reflect the views and policies of the funding agencies. Mention of trade names and commercial products does not constitute endorsement or recommendation for use.

Acknowledgements

This work was financially supported by the Ministry of Science and Technology of China (2016YFC0400802); National Natural Science Foundation of China (51878653, 21590814, 51525806); and the Youth Innovation Promotion Association of Chinese Academy of Sciences.

Appendix A. Supplementary data

Supplementary material related to this article can be found, in the online version, at doi:https://doi.org/10.1016/j.jhazmat.2019.121855.

References

Anipsitakis, G.P., Dionysiou, D.D., 2004. Radical generation by the interaction of transition metals with common oxidants. Environ. Sci. Technol. 38, 3705–3712.
Bedin, K.C., Martins, A.C., Cazetta, A.L., Pezoti, O., Almeida, V.C., 2016. KOH-activated carbon prepared from sucrose spherical carbon: adsorption equilibrium, kinetic and thermodynamic studies for methylene blue removal. Chem. Eng. J. 286, 476–484.
Bolton, J.R., 2006. Advanced Oxidation Handbook. American Water Works Association.
Bolton, J.R., Stefan, M.I., 2002. Fundamental photochemical approach to the concepts of fluence (UV dose) and electrical energy efficiency in photochemical degradation reactions. Res. Chem. Intermed. 28, 857–870.
Brezonik, P.L., Fulkerson-Brekken, J., 1998. Nitrate-induced photolysis in natural waters: controls on concentrations of hydroxyl radical photo-intermediates by natural scavenging agents. Environ. Sci. Technol. 32, 3004–3010.
Bulut, Y., Aydın, H., 2006. A kinetics and thermodynamics study of methylene blue adsorption on wheat shells. Desalination 194, 259–267.
Buxton, G.V., Greenstock, C.L., Helman, W.P., Ross, A.B., 1988. Critical review of rate constants for reactions of hydrated electrons, hydrogen atoms and hydroxyl radicals ($^{\bullet}OH/^{\bullet}O^-$) in aqueous solution. J. Phys. Chem. Ref. Data 17, 513–886.
Buxton, G.V., Barlow, S., McGowan, S., Salmon, G.A., Williams, J.E., 1999. The reaction of the $SO_3^{\bullet-}$ radical with Fe(II) in acidic aqueous solution-A pulse radiolysis study. Phys. Chem. Chem. Phys. 1, 3111–3115.
Canonica, S., Meunier, L., Von Gunten, U., 2008. Phototransformation of selected pharmaceuticals during UV treatment of drinking water. Water Res. 42, 121–128.
Crittenden, J.C., Hu, S.M., Hand, D.W., Green, S.A., 1999. A kinetic model for H_2O_2/UV process in a completely mixed batch reactor. Water Res. 33, 2315–2328.
Gao, Y.Q., Gao, N.Y., Deng, Y., Yang, Y.Q., Ma, Y., 2012. Ultraviolet (UV) light-activated persulfate oxidation of sulfamethazine in water. Chem. Eng. J. 195–196, 248–253.
Gilbert, B.C., Stell, J.K., 1990. Mechanisms of peroxide decomposition: an electron paramagnetic resonance study of the reaction of the peroxomonosulphate anion ($HOOSO_3^-$) with Cu^{I}. A marked contrast in behavior with that of Ti^{III} and Fe^{II}. J. Chem. Soc. Faraday Trans. 86, 3261–3266.
Gonzalez, M.G., Oliveros, E., Worner, M., Braun, A.M., 2004. Vacuum-ultraviolet photolysis of aqueous reaction systems. J. Photochem. Photobiol. 5, 225–246.
Guan, Y.H., Ma, J., Li, X.C., Fang, J.Y., Chen, L.W., 2011. Influence of pH on the formation of sulfate and hydroxyl radicals in the UV/peroxymonosulfate system. Environ. Sci. Technol. 45, 9308–9314.
Hori, H., Yamamoto, A., Hayakawa, E., Taniyasu, S., Yamashita, N., Kutsuna, S., Kiatagawa, H., Arakawa, R., 2005. Efficient decomposition of environmentally persistent perfluorocarboxylic acids by use of persulfate as a photochemical oxidant. Environ. Sci. Technol. 39, 2383–2388.
Hou, S.D., Ling, L., Dionysiou, D.D., Wang, Y.R., Huang, J.J., Guo, K.H., Li, X.C., Fang, J.Y., 2018. Chlorate formation mechanism in the presence of sulfate radical, chloride, bromide and natural organic matter. Environ. Sci. Technol. 52, 6317–6325.
Huang, F.M., Chen, L., Wang, H.L., Yan, Z.C., 2010. Analysis of the degradation mechanism of methylene blue by atmospheric pressure dielectric barrier discharge plasma. Chem. Eng. J. 162, 250–256.
Ike, I.A., Linden, K.G., Orbell, J.D., Duke, M., 2018. Critical review of the science and sustainability of persulphate advanced oxidation processes. Chem. Eng. J. 338, 651–669.
Jayson, G.G., Parsons, B.J., Swallow, A.J., 1973. Some simple, highly reactive, inorganic chlorine derivatives in aqueous solution. Their formation using pulses of radiation and their role in the mechanism of the Fricke dosimeter. J. Chem. Soc. Faraday Trans. 69, 1597–1607.
Kim, S.M., Vogelpohl, A., 1998. Degradation of organic pollutants by the photo-Fenton-process. Chem. Eng. Technol. 21, 187–191.
Kutschera, K., Bornick, H., Worch, E., 2009. Photoinitiated oxidation of geosmin and 2-methylisoborneol by irradiation with 254 nm and 185 nm UV light. Water Res. 43, 2224–2232.
Latch, D.E., McNeill, K., 2006. Microheterogeneity of singlet oxygen distributions in irradiated humic acid solutions. Science 311, 1743–1747.
Lau, T.K., Chu, W., Graham, N.J.D., 2007. The aqueous degradation of butylated hydroxyanisole by UV/$S_2O_8^{2-}$ study of reaction mechanisms via dimerization and mineralization. Environ. Sci. Technol. 41, 613–619.
Li, M.K., Qiang, Z.M., Hou, P., Bolton, J.R., Qu, J.H., Li, P., Wang, C., 2016. VUV/UV/chlorine as an enhanced advanced oxidation process for organic pollutant removal from water: assessment with a novel mini-fluidic VUV/UV photoreaction system (MVPS). Environ. Sci. Technol. 50, 5849–5856.
Li, M.K., Hao, M.Y., Yang, L.X., Yao, H., Bolton, J.R., Blatchley, E.R., Qiang, Z.M., 2018. Trace organic pollutant removal by VUV/UV/chlorine process: feasibility investigation for drinking water treatment on a mini-fluidic VUV/UV photoreaction system and a pilot photoreactor. Environ. Sci. Technol. 52, 7426–7433.
Lian, L.S., Yao, B., Hou, S.D., Fang, J.Y., Yan, S.W., Song, W.H., 2017. Kinetic study of hydroxyl and sulfate radical-mediated oxidation of pharmaceuticals in wastewater effluents. Environ. Sci. Technol. 51, 2954–2962.
Lian, J.F., Qiang, Z.M., Li, M.K., Bolton, J.R., Qu, J.H., 2015. UV photolysis kinetics of sulfonamides in aqueous solution based on optimized fluence quantification. Water Res. 75, 43–50.
Ling, L., Sun, J.L., Fang, J.Y., Shang, C., 2016. Kinetics and mechanisms of degradation of chloroacetonitriles by the UV/H_2O_2 process. Water Res. 99, 209–215.
McCallum, J.E.B., Madison, S.A., Alkan, S.A., Depinto, R.L., Rojas Wahl, R.U., 2000. Analytical studies on the oxidative degradation of the reactive textile dye Uniblue A. Environ. Sci. Technol. 34, 5157–5164.
Mckay, G., Dong, M.M., Kleinman, J.L., Mezyk, S.P., Rosario-Ortiz, F.L., 2011. Temperature dependence of the reaction between the hydroxyl radical and organic matter. Environ. Sci. Technol. 45, 6932–6937.
Neta, P., Huie, R.E., Ross, A.B., 1988. Rate constants for reactions of inorganic radicals in aqueous solution. J. Phys. Chem. Ref. Data 17, 1027–1284.
O'Neill, P., Steeken, S., Schulte-Frohlinde, D., 1975. Formation of radical cations of methoxylated benzenes by reaction with OH radicals, Ti^{2+}, Ag^{2+}, and $SO_4^{\bullet-}$ in aqueous solution. An optical and conductometric pulse radiolysis and in situ radiolysis electron spin resonance study. J. Phys. Chem. 79, 2773–2779.

Pan, B., Zhou, Y.G., Su, W.Y., Wang, X.X., 2017. Self-assembly synthesis of $LaPO_4$ hierarchical hollow spheres with enhanced photocatalytic CO_2-reduction performance. Nano Res. 10, 534–545.
Qi, J.Q., Li, X.C., Zheng, H., Li, P.Q., Wang, H.Y., 2015. Simultaneous removal of methylene blue and copper(II) ions by photoelectron catalytic oxidation using stannic oxide modified iron(III) oxide composite electrodes. J. Hazard. Mater. 293, 105–111.
Rao, P.S., Hayon, E., 1973. Experimental determination of the redox potential of the superoxide radical $^{\bullet}O_2^-$. Biochem. Biophys. Res. Commun. 51, 468–473.
Rastogi, A., Ai-Abed, S.R., Dionysiou, D.D., 2009. Sulfate radical-based ferrous-peroxymonosulfate oxidative system for PCBs degradation in aqueous and sediment systems. Appl. Catal. B-Environ. 85, 171–179.
Ren, Y., Li, T., Zhang, W.M., Wang, S., Shi, M.Q., Shan, C., Zhang, W.B., Guan, X.H., Lv, L., Hua, M., Pan, B.C., 2019. MIL-PVDF blend ultrafiltration membranes with ultrahigh MOF loading for simultaneous adsorption and catalytic oxidation of methylene blue. J. Hazard. Mater. 365, 312–321.
Tang, W.Z., Huang, C.P., 1996. 2,4-dichlorophenol oxidation kinetics by Fenton's reagent. Environ. Technol. 17, 1371–1378.
Thayer, A., 2003. Fighting SARS-Common disinfectants may slow SARS. Chem. Eng. News 81, 9.
Von Gunten, U., 2003. Ozonation of drinking water: part II. Disinfection and by-product formation in presence of bromide, iodide or chlorine. Water Res. 37, 1469–1487.
Waldemer, R.H., Tratnyek, P.G., Johnson, R.L., Nurmi, J.T., 2007. Oxidation of chlorinated ethenes by heat-activated persulfate: kinetics and products. Environ. Sci. Technol. 41, 1010–1015.
Weiner, E.R.A., 2000. Dictionary of inorganic water quality parameters and pollutants. Applications of Environmental Chemistry, A Practical Guide for Environmental Professionals, Chapter 7. Lewis, Florida.
Wen, D., Wu, Z.D., Tang, Y.B., Li, M.K., Qiang, Z.M., 2018. Accelerated degradation of sulfamethazine in water by VUV/UV photo-Fenton process: impact of sulfamethazine concentration on reaction mechanism. J. Hazard. Mater. 344, 1181–1187.
Wolski, L., Ziolek, M., 2018. Insight into pathways of methylene blue degradation with H_2O_2 over mono and bimetallic Nb, Zn oxides. Appl. Catal. B-Environ. 224, 634–647.
Xie, P.C., Ma, J., Liu, W., Zou, J., Yue, S.Y., Li, X.C., Wiesner, M.R., Fang, J.Y., 2015. Removal of 2-MIB and geosmin using UV/persulfate: contributions of hydroxyl and sulfate radicals. Water Res. 69, 223–233.
Yang, Y., Pignatello, J.J., Ma, J., Mitch, W.A., 2014. Comparison of halide impacts on the efficiency of contaminant degradation by sulfate and hydroxyl radical-based advanced oxidation processes (AOPs). Environ. Sci. Technol. 48, 2344–2351.
Zhang, T., Hsu-Kim, H., 2010. Photolytic degradation of methylmercury enhanced by binding to natural organic ligands. Nat. Geosci. 3, 473–476.
Zhang, R.C., Yang, Y.K., Huang, C.H., Zhao, L., Sun, P.Z., 2016. Kinetics and modeling of sulfonamide antibiotic degradation in wastewater and human urine by UV/H_2O_2 and UV/PDS. Water Res. 103, 283–292.
Zoschke, K., Bornick, H., Worch, E., 2014. Vacuum-UV radiation at 185 nm in water treatment – a review. Water Res. 52, 131–145.